

## Article

# Computationally Inexpensive CFD Approach for the Combustion of Sewage Sludge Powder, Including the Consideration of Water Content and Limestone Additive Variations

Benjamin Ortner <sup>1,\*</sup>, Christian Schmidberger <sup>2</sup>, Hannes Gerhardtter <sup>1</sup>, René Prieler <sup>1</sup>, Hartmuth Schröttner <sup>3</sup> and Christoph Hochenauer <sup>1</sup>

<sup>1</sup> Institute of Thermal Engineering, Faculty of Mechanical Engineering and Economic Sciences, Graz University of Technology, Inffeldgasse 25B, 8010 Graz, Austria

<sup>2</sup> Institute of Combustion and Power Plant Technology, Faculty 4-Energy-, Process- and Bio-Engineering, University of Stuttgart, Pfaffenwaldring 23, 70569 Stuttgart, Germany

<sup>3</sup> Austrian Centre for Electron Microscopy and Nanoanalysis, Steyrergasse 17, 8010 Graz, Austria

\* Correspondence: benjamin.ortner@tugraz.at

**Abstract:** As a result of growing interest in the thermal treatment of sewage sludge with methods such as combustion, gasification or pyrolysis, and also in processes that aim to recover precious components such as phosphorus from this waste, a growing demand has been observed for Computational Fluid Dynamics (CFD) models that provide solutions rapidly and accurately for efficient application in research and development. This study was carried out to develop a computationally inexpensive modelling approach for the combustion of pulverized sewage sludge in entrained flow furnaces. Sewage sludge is a very volatile-rich fuel. Therefore, the Steady Diffusion Flamelet model (SFM), in combination with a validated skeletal reaction mechanism, was applied to consider the pulverized firing of sewage sludge. It was possible to represent the complex composition of volatiles emitted from the sludge particles by releasing surrogate fuels. In addition, the influence of limestone additive (calcination reaction) and varying water content (water–gas shift reaction) was investigated experimentally and modelled via CFD. The simulation results confirm that the surrogate fuel approach is valid and can be used to describe pulverized sewage sludge effectively. The temperature and species concentration results, including the influence of the additive and different levels of water content, were confirmed by experimental data, which is usually hard to obtain due to the tendency of PSS to form agglomerates in entrained flow combustion furnaces. The model yields plausible and experimentally validated results for the combustion of sewage sludge powder across a wide range of operating conditions.

**Keywords:** sewage sludge combustion; flamelet modelling; entrained flow furnace



**Citation:** Ortner, B.; Schmidberger, C.; Gerhardtter, H.; Prieler, R.; Schröttner, H.; Hochenauer, C. Computationally Inexpensive CFD Approach for the Combustion of Sewage Sludge Powder, Including the Consideration of Water Content and Limestone Additive Variations. *Energies* **2023**, *16*, 1798. <https://doi.org/10.3390/en16041798>

Academic Editor: Rob J.M. Bastiaans

Received: 2 January 2023

Revised: 31 January 2023

Accepted: 7 February 2023

Published: 11 February 2023



**Copyright:** © 2023 by the authors. Licensee MDPI, Basel, Switzerland. This article is an open access article distributed under the terms and conditions of the Creative Commons Attribution (CC BY) license (<https://creativecommons.org/licenses/by/4.0/>).

## 1. Introduction

With a growing world population and steadily increasing hygiene standards, greater amounts of municipal waste can be expected in the future. Sewage sludge has often been directly used in agricultural activities in the past. Currently, this way of utilizing the material is considered increasingly problematic, since it also contains various harmful materials such as heavy metals, as reported by Udayanga et al. [1].

Sewage sludge is a waste product that contains a significant amount of energy. Therefore, it is often used in co-incineration processes together with municipal waste, according to Roy et al. [2], or together with pulverized coal, as studies from Namkung et al. [3] and Stelmach et al. [4] report. Bianchini et al. [5] reported a rising interest in thermal treatments, such as gasification, as a method of sewage sludge disposal and valorization

in the European Union. Quan et al. [6] provided a recent review on the application of gasification and combustion technology in sewage sludge treatment.

Furthermore, sewage sludge can be a source of essential elements such as phosphorus, which can be recovered in the sense of a circular economy [7]. This aspect is especially interesting in Europe, which is heavily dependent on the importation of such materials [8]. One starting point for the energy-intensive recovery process of phosphorus from sewage sludge is a conversion process that harnesses the energy content present in the pulverized sewage sludge (PSS-sewage sludge after drying and grinding).

Computational fluid dynamics (CFD) simulations are often employed as a method applied in research and development. For this reason, a new numerically inexpensive modelling approach, developed as part of this research, is presented in this study.

### 1.1. Combustion and Gasification Modelling of Pulverized Sewage Sludge

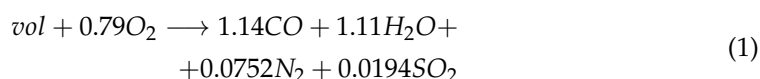
In an early study, Wang et al. [9] noted that the PSS combustion process can be closely compared to that of pulverized coal combustion. Both coal and PSS contain considerable mass fractions of water, volatile matter, fixed carbon and ash. The major relations between lignite and PSS are summarized in Table 1. Assessing PSS from this point of view, it can be classified as a volatile-rich and high-ash fuel. While the organic contents of the material are most relevant for the combustion process, the sewage sludge ash can serve as a raw material for further processing, such as phosphorus recovery [7].

**Table 1.** Comparison of PSS particles to lignite and order of magnitude for particle properties.

Feature	Comparison to Coal	Mass Fraction PSS
Water content	generally higher for PSS, low in our case due to effective pre-drying	<20%
Volatile release	generally higher for PSS, much higher in our case	>40%
Fixed carbon	generally lower for PSS, much lower in our case	<4%
Ash (slag)	generally higher for PSS, very high in our case	>40%

The relatively high ash content in PSS results in it having a small lower heating value (LHV) of around 12 MJ/kg (on a dry basis) [10]; on a wet basis and with water content beyond 60% (wet sludge), this value can even be negative [11]. For this reason, the focus of this study lies on pre-dried sewage sludge.

Generally, the volatiles emitted from PSS particles do not consist of only one species. In solid fuel combustion modelling, they are often considered with two main reaction steps. For instance, in reaction Equation (1), the term *vol* stands for the averaged composition of the volatiles. This can be derived from the ultimate analysis of the fuel and will usually have complex formulae, such as  $C_{1.14}H_{2.23}O_{0.70}N_{0.1504}S_{0.0194}$  (Example based on the sewage sludge powder used in this study). In this first step, besides  $H_2O$  and  $SO_2$ , the reaction product  $CO$  is formed. In a second step, reaction Equation (2), the  $CO$  further reacts to the final reaction product  $CO_2$ .



Early CFD-related studies, such as that by Fletcher et al. [12], used one- or two-step reaction mechanisms and the Eddy dissipation model (EDM) to consider the combustion chemistry in their CFD models. Years later, in publications such as that of Lin et al. [13], this approach is still being successfully used. To this day, this approach is also popular in indus-

try, as it can be simply applied and provides solutions rapidly. Understandably, detailed finite-rate chemistry data are not universally available for such simplified approaches. This is one of the main motivations behind this study: The inclusion of detailed chemistry in the CFD combustion simulations of a complex fuel with many uncertain properties.

A more accurate surrogate fuel approach for sewage sludge conversion has already been proposed by Znidarcic et al. [14]. Therein, detailed and validated reaction mechanisms are used to describe the combustion of either experimentally or analytically determined compositions of volatiles based on well-defined species, such as methane, ethanol, heptane etc. However, these authors applied highly detailed reaction mechanisms with more than 2500 reversible reactions on a relatively simple computational domain in order to consider the chemical kinetic effects in small-scale sludge incineration plants in more detail. They later updated the CFD model to feature reduced chemical mechanisms, as reported in their second publication [15]. Detailed chemistry considerations like these can be achieved by means of the Eddy Dissipation Concept (EDC) approach, which is well-established today, even for large-scale systems, but is then often limited to a small number of chemical reactions.

The high computational costs associated with detailed chemistry considerations can be alleviated by maintaining the surrogate approach and applying the Steady Diffusion Flamelet (SFM) model. The idea of using an SFM-based surrogate approach for more complex fuels, such as biomass, has already successfully been applied by Buchmayr et al. [16,17]. These authors proposed using computationally inexpensive CFD models for biomass burners equipped with enhanced air-staging. However, they did not focus on pulverized fuels such as coal or PSS but rather on grate furnaces [18].

Watanabe et al. [19] developed a flamelet-based CFD-model for coal combustion by introducing a two-mixture-fraction approach. In this way, the volatile combustion (in their study composed of CO, CH<sub>4</sub> and C<sub>2</sub>H<sub>2</sub>) and char burnout can be accurately considered. Wen et al. [20] also used a two-mixture-fraction Flamelet model for the numerical simulation of pulverized coal combustion while considering larger particle sizes and their influence on flame characteristics.

The combustion and gasification of pulverized fuels involves a devolatilization process, which has been investigated in detail by many researchers, including Mularski et al. [21,22] for coal and Zhu et al. [23] for sewage sludge. As highlighted by Fletcher et al. [12], devolatilization is a highly complex and uncertain process. According to Merabian et al. [24], the volatile composition depends on the heating rate and temperature levels. The yield of volatile matter increases as the temperatures rise, as described by Kobayashi et al. [25]. The main components, however, are always tars, CO<sub>2</sub>, CO, H<sub>2</sub>O, H<sub>2</sub>, CH<sub>4</sub> and C<sub>n</sub>H<sub>m</sub>. This finding has been confirmed for sewage sludge via experimental studies such as those carried out by Schmid et al. [26].

Detailed chemistry calculations involving gas-phase reactions with complex reaction mechanisms and detailed particle kinetics can be computationally demanding. Therefore, they are not very useful for the development of large-scale sewage sludge conversion systems, which can have complex geometries and thus require a high number of computational cells to resolve the domain.

## 1.2. Objective of This Paper

This study was carried out to develop a computationally inexpensive, steady-state simulation approach that can be used when designing full-scale sewage sludge conversion furnaces. The simulation model aims to combine the surrogate fuel approach of Znidarcic et al. [14] with a particle physics model in order to facilitate the accurate prediction of temperatures and flue gas concentrations in pulverized sewage sludge conversion furnaces. A skeletal reaction mechanism applied in a Steady Diffusion Flamelet (SFM) approach was included to improve the predictions by considering non-equilibrium effects while maintaining numerical efficiency. This study thereby focuses on the gas phase reactions, since the fixed carbon content is low, and particle conversion occurs rapidly. This is supported

by high temperatures in the furnace and very small particle sizes. Detailed particle-kinetic effects are therefore only relevant very close to the burner inlet, where measurements are infeasible. More details on combustion modelling can be found in Section 2.3.3. Having a clear understanding of the turbulent flow and having an accurate prediction model of the atmosphere in such a system available can accelerate the development of the respective plants and their components. The accurate prediction of the thermophysical process in a furnace is especially relevant when particle reduction effects must be avoided. This is the case for furnaces where a pulverized fuel will be combusted or gasified for further processing (e.g., for phosphorus recovery processes from sewage sludge slag).

## 2. Materials and Methods

In this section, the considered material and the experiment that enabled us to obtain the measurement data are briefly explained. These data were then used to test the CFD models.

### 2.1. Material Properties

The elementary and proximate analysis results are shown in Table 2. The high ash and volatile content is typical for PSS. The fixed carbon fraction is very low as compared to that of lignite, where it can exceed >40 to 50%, as studies by Al-abbas [27] and Steibel [28] have shown.

**Table 2.** Elementary and proximate analysis of the considered PSS, daf = dry, ash-free.

Elementary Analysis	Mass Fraction Daf	Proximate Analysis	Mass Fraction
C	0.508	Water content	0.100
H	0.068	Volatile matter	0.409
O	0.341	Fixed carbon	0.041
N	0.064	Ash	0.450
S	0.019		

The sewage sludge was pre-dried and ground. A detailed particle size distribution (PSD), as well as particle shape information, was determined using dynamic image analysis (DIA). The result is displayed in Figure 1, marked with crosses. The PSD seems to be bimodal, with the vast majority of the particle mass consisting of particles with smaller sizes than 100  $\mu\text{m}$ . Nevertheless, PSD is quite wide, which can be explained by fibrous material that causes spikes at the high end of the distribution.

The overwhelming majority of particles exhibit sphericities in the 0.7–0.8 range, defined according to Wadell (1932). This is confirmed by scanning electron microscopy (SEM) imaging, as displayed in Figure 2, which shows some large and fine particles and their rough surface.

In the thermogravimetric analyser (TGA) measurements, at 10 K/min, the sewage sludge probes demonstrated a gradual mass loss over a wide temperature range, as shown in Figure 3a. The mass loss effect began at temperatures below 100  $^{\circ}\text{C}$ , indicating the drying and evaporation of the water content. After all of the volatile components were released from the particle and the char conversion was finished, around 42% of the original particle mass remained as ash (slag). Figure 3b shows a Factsage-calculated, temperature-dependent specific heat curve for the PSS ash, as used in the simulations. The slope of this curve gradually increases as the temperatures rise and includes peaks which represents the melting effect in a simplified way. The initial particle density was determined as 1840  $\text{kg}/\text{m}^3$  with a helium pycnometer. The thermal conductivity of the particles was set to a constant value of 1.0  $\text{W}/(\text{m} \cdot \text{K})$ , which is a reasonable estimate for ash particles [29]. These material properties were used in the CFD simulations.

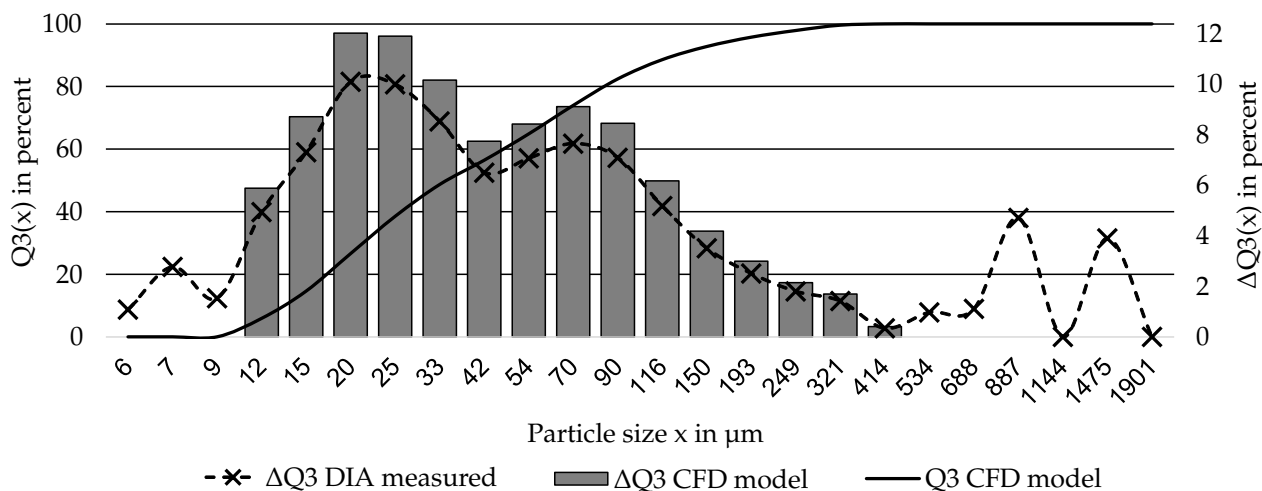


**Figure 1.** Particle size distribution. The grey columns represent classes as defined in the CFD simulations, which mass-wise include fine and large particle (fibers) fractions.

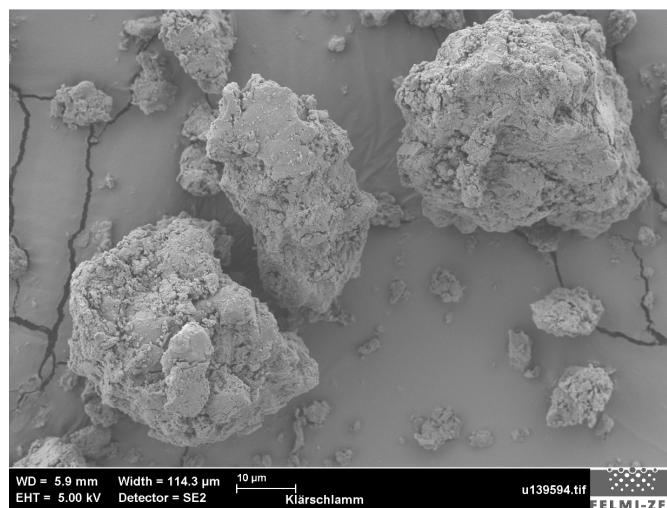


**Figure 2.** SEM image of PSS particles.

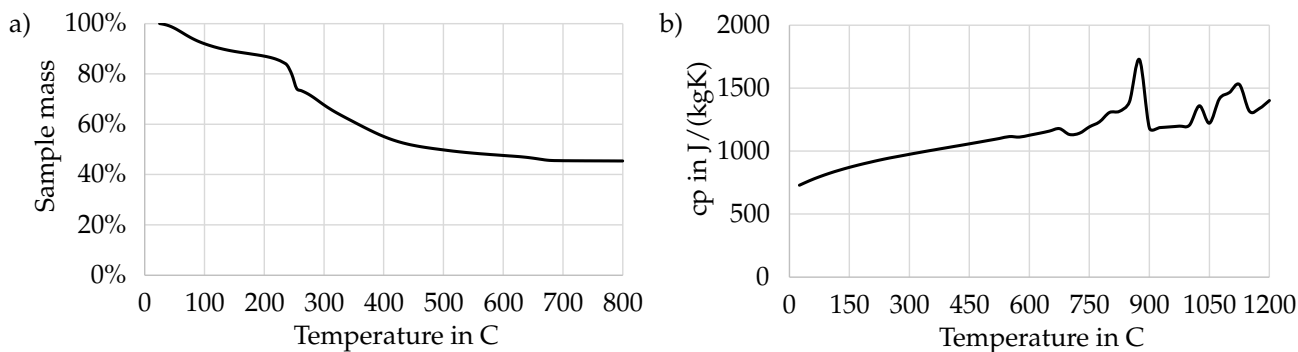


**Figure 3.** Material properties (a) TGA curve at 10 K/min, (b) Specific heat capacity of the PSS particles.

*2.2. Experimental Furnace Operation*

The furnace under consideration is a top-fired entrained flow gasifier consisting of a 2.5-m-long combustion chamber with electrically heated walls (see Figure 4). Using this setup, the conditions in an industrial combustion reactor can be accurately replicated.

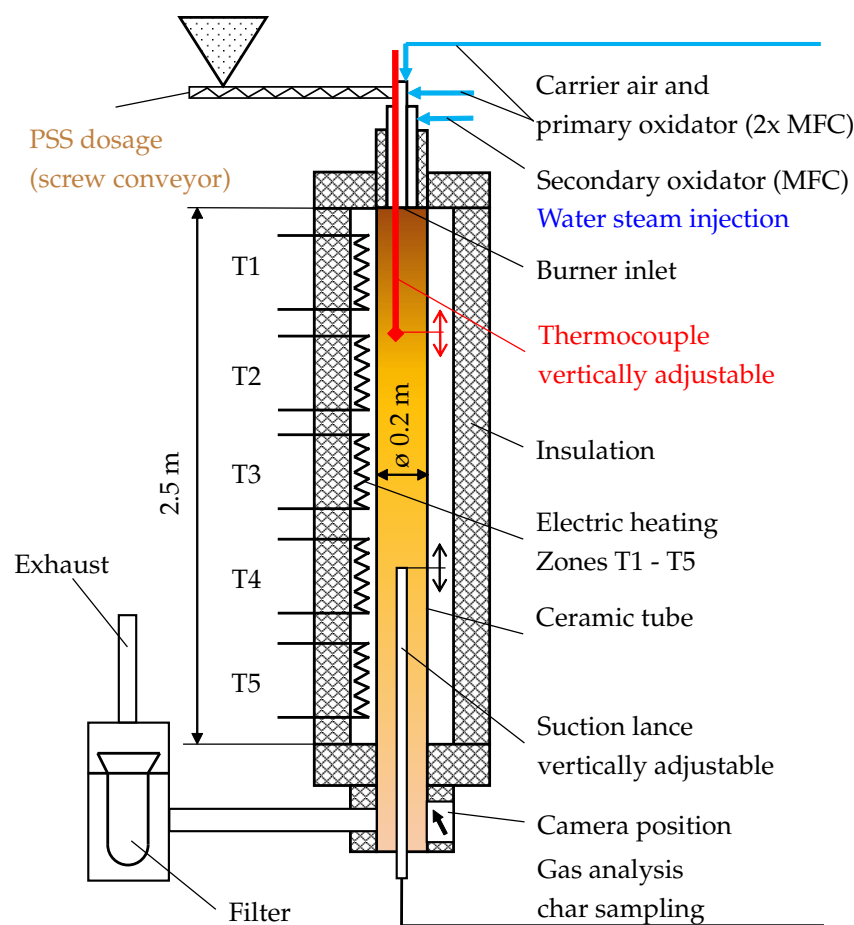


Figure 4. Experimental reactor

The equivalence ratio (ER) and oxygen-enhancement levels were set and controlled using three mass flow controllers (MFC) for the oxidator flows and a screw conveyor for the pulverized fuel dosage. It was not feasible to prepare large enough PSS probes with accurate varying water contents. Therefore, the varying PSS water contents were replicated in the experiment by injecting the corresponding amount of steam through the annular pipe, which is the secondary oxidator inlet. The PSS as received (ar) has a water content 10% according to Table 2. Therefore, since 3 kg/h of PSS are considered, 150 g/h and 300 g/h were injected to simulate water contents of roughly 15% and 20% for the PSS. Higher water contents were not considered, since the PSS material tends to clog at these levels, which would impede accurate dosage in reality.

The wall temperature was set to constant 1300 °C through electric heating, which enabled steady-state combustion to be achieved even at low fuel mass flow rates. These were necessary to delay the slagging-related obstruction of the vertically adjustable suction lance used for flue gas measurements and particulate matter sampling.

### Measurements

The flue gas composition was measured using the vertically adjustable suction lance indicated in Figure 4. Particle probes were additionally taken with this appliance. Measurements were performed at a distance of 1.5 m from the burner inlet. CO, CO<sub>2</sub>, O<sub>2</sub>, H<sub>2</sub> and CH<sub>4</sub> measurements (dry-based) were taken at this distance to determine the flue gas composition since no changes were detectable further from the inlets.

During gas sampling, slagging due to the high ash content in the PSS was observed. Figure 5 shows the effect of slagging; the differences between Figure 5a,c are caused by only a few minutes of operation at low fuel mass flows of around 3 kg/h. Closer than the aforementioned 1.5 m to the burner, measurements tended to become unstable and

inaccurate. Nevertheless, successful equilibrium measurements were possible, and these were subsequently used to test the CFD model results.

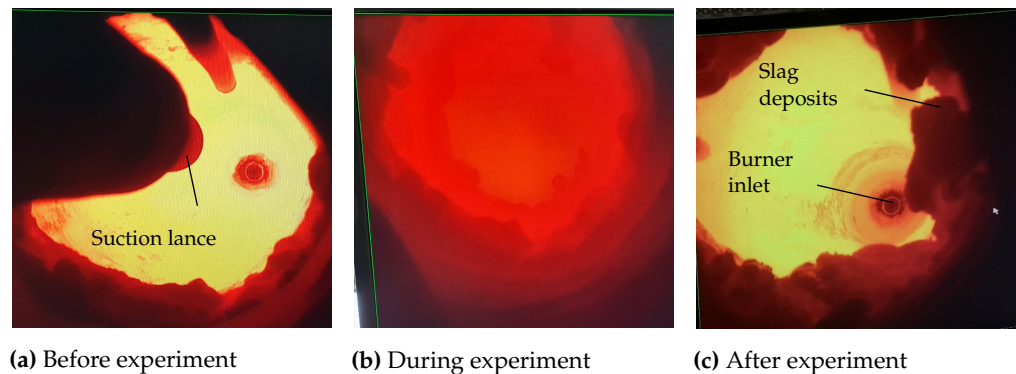


**Figure 5.** View from the bottom of the reactor towards the burner inlet showing slagging due to the high-ash content of the fuel. The direction of the view is indicated in Figure 4 as “Camera position”.

Temperature measurements close to the burner were performed using a vertically adjustable thermocouple (TC), which was inserted from the top and extended down to a maximum distance of 0.4 m from the burner.

### 2.3. Numerical Setup

In this section, the CFD modelling of the system is explained in detail. This includes a description of the computational domain and basic information about mathematical modelling, as well as the chemistry and radiation modelling approaches. All numerical calculations were performed using the commercial software code *ANSYS Fluent 2020 R2*.

#### 2.3.1. Computational Domain

One-third of the reactor geometry was meshed, taking advantage of a 120°-periodic system and by applying corresponding periodic boundary conditions. A further simplification to a 2D-problem is not possible since the burner uses three distinct high-velocity nozzles around the circumference to inject the majority of the oxidator gas. This delivers the majority of the momentum flux to the domain. In total, 456,945 hexahedral and a few wedge-type cells were used to form the computational mesh, as shown in Figure 6. A maximum skewness of 0.70 with an average value below 0.08 and a minimal orthogonal quality of 0.59 with an average value of 0.98 were achieved.

A mesh independence study was carried out using a coarser mesh with 93,620 hexahedral/wedge cells and a finer mesh with 2,167,420 hexahedral/wedge cells. Only slight differences were observed between the standard mesh and the fine mesh, depicted in Figure 7. In fact, the coarser mesh also produced highly similar results. From this point of view, the results can be considered mesh-independent.

However, it was noticed that the number of trapped particles changes with the mesh resolution, as depicted in Figure 8. The coarse mesh predicted many more particles becoming trapped at the heated walls than the two finer meshes, which is why the medium-sized mesh is used in all further considerations.

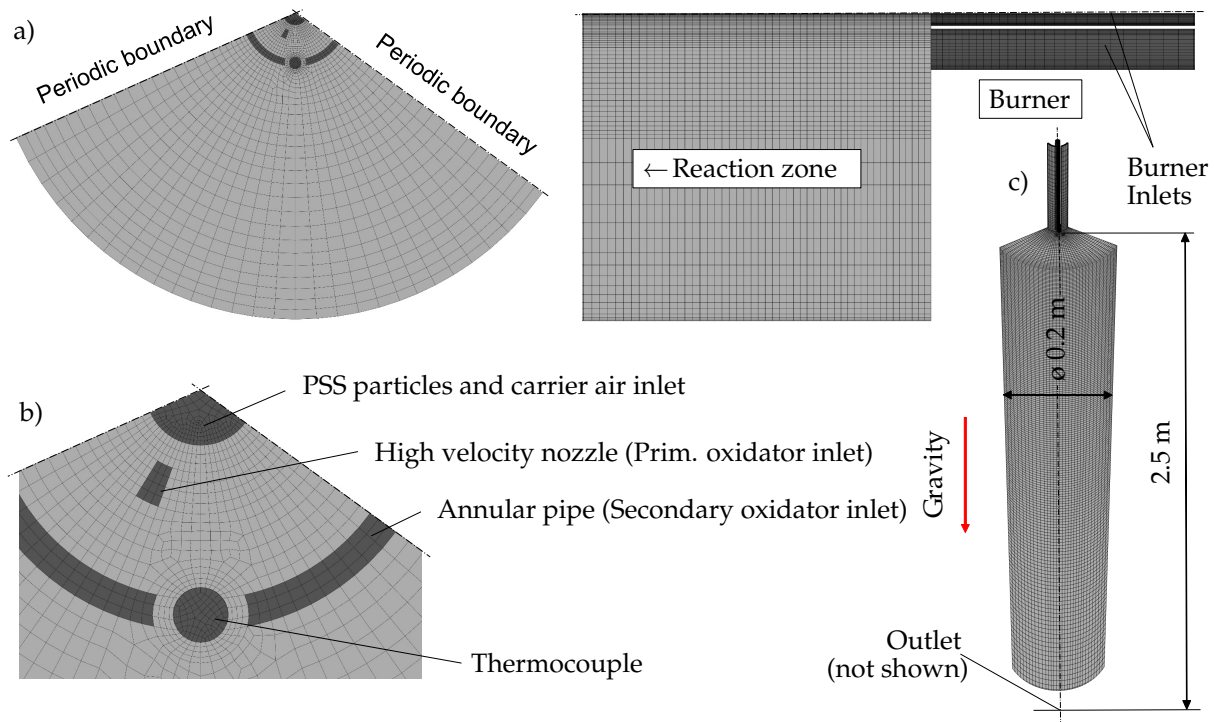


**Figure 6.** Computational domain-(a) Top and lateral view (b) Detailed view of inlets (c) Isometric view of the first 1.0 m.

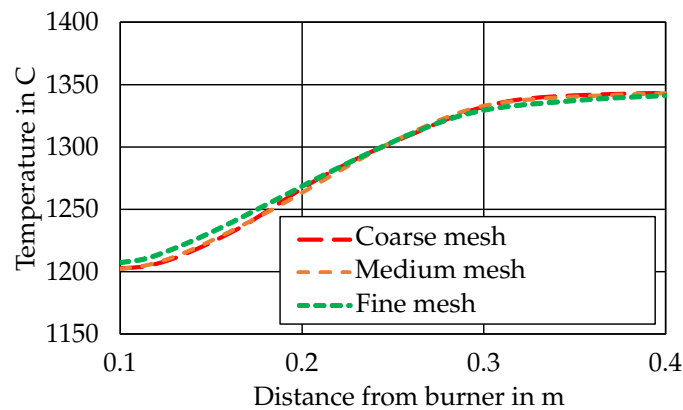


**Figure 7.** Temperature profile along the thermocouple axis with grid independence study, Case 1.

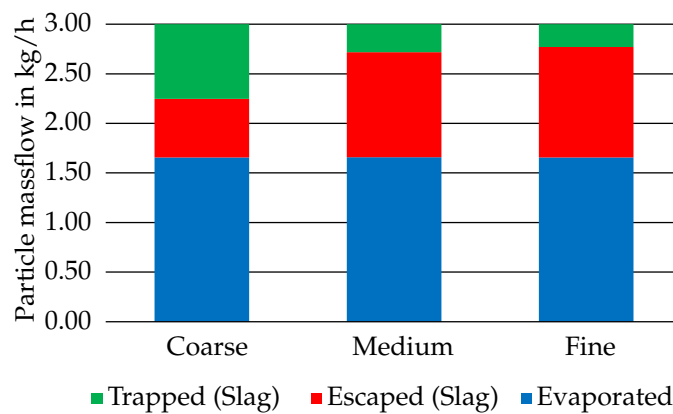


**Figure 8.** Grid independence study, particle balance for Case 1.



### 2.3.2. Particle-Laden Flow

The turbulent flow in the experimental reactor was calculated by determining steady-state solutions for the Favre-averaged Navier–Stokes equations using a pressure-based solver. The temperature-dependent density was considered using the incompressible ideal gas law. Polynomial approaches were taken to include the temperature-dependent specific heat, thermal conductivity and viscosity of the gas mixture.

Turbulence was modelled using the k-omega-SST model by Menter [30]. It is suitable for modelling the transition from the high velocities near the burner inlets to the extremely low velocities expected close to the heated walls of the combustion chamber. This approach was recommended for the same reasons by Christ [31], especially regarding furnace modelling.

It was necessary to consider Lagrangian particle tracking, including two-way coupling with the continuous phase, since the location where the devolatilization of PSS takes place influences the flame position. This was achieved by applying the Discrete Phase Model (DPM). A particle track calculation was performed every 25 fluid iterations and involved the consideration of at least 12,000 single particle tracks. No difference in the results was observed after increasing the number of calculated particle tracks even further. Stochastic tracking was implemented by means of the Discrete Random Walk model with a time scale constant of 0.15 and enabling random eddy lifetimes.

The particles were considered non-spherical according to SEM images and DIA measurements as described above. Drag force ( $F_D$ ) calculations for the force balance Equation (3), using the definition of the drag force according to Equation (4) and the drag coefficient  $c_D$  according to Equation (5), were performed using the correlations of Haider–Levenspiel et al. [32]. These correlations enabled the coefficients  $b_1$ – $b_4$  to be obtained. The definition of the particle Reynolds number of a spherical particle  $Re_{sph}$  is given with Equation (6). A sphericity ( $\psi = s/S$ , where in  $s$  is the surface area of a sphere having the same volume as the particle, and  $S$  is the actual surface area of the particle. The coefficients  $b_1$ – $b_4 = f(\psi)$  can be found in the original publication [32]).  $\psi = 0.8$  was considered sufficient to describe the drag on the largest particles in the system. In general, the considered particles are very small, and the Stokes number is low ( $St \ll 1$ ), indicating that particles will follow the fluid flow quite accurately. In the equations below,  $d_p$  is the particle diameter,  $u_p$  is the particle velocity, and  $u$  is the velocity of the fluid. Likewise, the particle density is  $\rho_p$ , and the fluid density is  $\rho$ . Gravity  $g$  and fluid viscosity  $\mu$  also play roles in the particle track calculations.

$$\frac{du_p}{dt} = F_D(u - u_p) + \frac{g(\rho_p - \rho)}{\rho_p} \quad (3)$$

$$F_D = \frac{18\mu}{\rho_p d_p^2} \frac{c_D Re}{24} \quad (4)$$

$$c_D = \frac{24}{Re_{sph}} \left( 1 + b_1 Re_{sph}^{b_2} \right) + \frac{b_3 Re_{sph}}{b_4 + Re_{sph}} \quad (5)$$

$$Re_{sph} = \frac{\rho d_p |u_p - u|}{\mu} \quad (6)$$

With this approach, particle shape information beyond standard correlations for spherical particles is considered in the model. Due to the aforementioned reasons, mainly the small particle sizes, an even more detailed description of the particle shapes can be safely omitted, supporting the main focus of this study: a numerically inexpensive CFD model.

The heat transfer to the particles is a result of thermal radiation and convective heat transfer. The latter was considered by applying the correlation of Ranz et al. [33]

according to the following energy balance Equation (7) and the Nusslet number correlation in Equation (8).

$$m_p c_p \frac{dT_p}{dt} = A_p \left\{ - \left[ h + \epsilon_p \sigma T_p^3 \right] T_p + \left[ h T_\infty + \epsilon_p \sigma \Theta_R^4 \right] \right\} \quad (7)$$

$$Nu = \frac{h d_p}{k_\infty} = 2.0 + 0.6 Re_d^{1/2} Pr^{1/3} \quad (8)$$

Therein,  $m_p$  stands for the particle mass, and  $c_p$  is the specific heat capacity of the particle according to Figure 3b.  $T_p$  is the particle temperature, and  $A_p$  is its surface area. Furthermore,  $h$  is the heat transfer coefficient,  $\sigma$  is the Stefan–Boltzmann constant,  $k_\infty$  is the thermal conductivity, and  $Pr$  the Prandtl number ( $c_p \mu / k_\infty$ ) of the continuous phase. A particle emissivity of  $\epsilon_p = 0.9$  was used. Due to the small particle size, the Biot number, defined according to Equation (9), wherein  $V_p$  is the particle volume and  $\lambda_p$  its thermal conductivity (material property), is very low ( $Bi \ll 0.1$ ); therefore, inter-particle temperature gradients were omitted.

$$Bi = \frac{h V_p}{A_p \lambda_p} \quad (9)$$

### 2.3.3. Combustion Modelling

The key aspect of this study is the fact that PSS conversion is modelled by applying an SFM-based, non-premixed combustion model—a mixture fraction approach—as briefly described in this section.

The most important requirement for the application of a non-premixed combustion approach to be accurate, is that the most significant part of the chemical PSS conversion process is a matter of gas-phase reactions. Indeed, sewage sludge has some properties that render this modelling choice viable. Ogada et al. describe the combustion characteristics of sewage sludge in a fluidized bed as characterized by the fact that 90% of the ash-free components are released as volatiles [34]. They further describe the combustion characteristics of sewage sludge as close to that of gaseous fuels [35]. Cui et al. noted that dehydration and devolatilization of particles can take place simultaneously [36].

What supports the application of a non-premixed combustion approach further for our case, are the very small particle sizes and the high temperature atmosphere in the experimental reactor. Moreover, TGA curves such as in Figure 3a are usually determined at very low heating rates of 10–20 K/min, whereas the real heating rates in our reactor exceed  $10^5$  K/min. This forces the particles to devolatilize very quickly.

Instead of using an Eddy dissipation model (or EDC), where separate species transport equations have to be solved, a surrogate fuel will be defined in this study, which matches the chemical composition of the PSS as closely as the underlying skeletal reaction mechanism allows. This approach was already successfully applied by Buchmayr et al. [16] for biomass furnaces. These authors reported a massively reduced calculation time when using the SFM approach while maintaining a similar accuracy as in their EDC models.

For the SFM-based models described in this study, the mass fractions of 0.409 (volatile matter), 0.100 (water content) and 0.041 (fixed carbon) in Table 2 have to be combined into one apparent devolatilization species: the surrogate fuel. This approach was considered justified under the following assumptions:

- The volatile fraction of the fuel is very high. Together with water evaporation, close to 60% of the initial particle mass leaves the particle in the form of a released volatile.
- The fixed carbon mass fraction is relatively low in the considered PSS. Therefore, char combustion/gasification also occurs rapidly and can be included in the single mixture fraction, surrogate fuel approach.

- The particles can be safely considered thermally thin. They are of such a small size that no inter-particle temperature gradients need to be considered (Biot number  $Bi \ll 0.1$ ).
- The high temperatures in the furnace promote fast drying and devolatilization, where the release of distinct off-gasses from a particle cannot meaningfully be distinguished from one another (e.g.,  $\text{CO}_2$  from  $\text{CO}$  release). This is further supported by Cui et al. [36], who report that pyrolysis can even happen simultaneously with drying.

These assumptions are valid for the case of PSS combustion and gasification in the considered furnace. With these considerations in mind, and under the assumption of equal diffusion rates for all elements, a single mixture fraction  $f$  as shown in Equation (10) is defined, where  $Z_i$  is the elemental mass fraction for element  $i$ . The subscript  $ox$  denotes the value at the oxidizer stream inlet, and the subscript  $fuel$  denotes the value at the fuel stream inlet. Only two transport equations for the Favre-averaged mean mixture fraction  $\bar{f}$  (Equation (11)) and its variance  $\overline{f'^2}$  (Equation (12)) have to be solved. Although the surrogate fuel is gradually emitted from particles, the problem to be solved can be considered a non-premixed combustion case, since the particles represent a source term solely for the surrogate fuel within the fluid domain ( $S_m$  in Equation (11)). The thermochemistry calculation was performed prior to the actual CFD simulation and stored in look-up tables under the assumption of either chemical equilibrium for the conventional chemical equilibrium model (CEQ) or the use of the Flamelet calculations based on the heptane42.che reaction mechanism [37]. It includes 18 species and 42 reversible, homogeneous reactions. Possible fuel species for the surrogate fuel approach are:  $\text{H}_2$ ,  $\text{H}_2\text{O}$ ,  $\text{CO}$ ,  $\text{CO}_2$ ,  $\text{N}_2$ ,  $\text{C}_3\text{H}_6$  and  $\text{C}_7\text{H}_{16}$  to consider tars. The heptane approach is elegant, given that it enables us to consider the effect of long-chain hydrocarbons in the form of heptane as a component of the surrogate fuel. The definition of the boundary species (PSS surrogate fuel) is described in Section 2.3.6.

$$f = \frac{Z_i - Z_{i,ox}}{Z_{i,fuel} - Z_{i,ox}} \quad (10)$$

$$\frac{\partial}{\partial t} (\rho \bar{f}) + \nabla \cdot (\rho \vec{v} \bar{f}) = \nabla \cdot \left( \frac{\mu_t}{\sigma_t} \nabla \bar{f} \right) + S_m \quad (11)$$

$$\begin{aligned} \frac{\partial}{\partial t} (\rho \overline{f'^2}) + \nabla \cdot (\rho \vec{v} \overline{f'^2}) = \\ \nabla \cdot \left( \frac{\mu_t}{\sigma_t} \nabla \overline{f'^2} \right) + C_g \mu_t (\nabla \bar{f})^2 - C_d \rho \frac{\epsilon}{k} \overline{f'^2} \end{aligned} \quad (12)$$

In Equations (11) and (12), the constants are set to  $\sigma_t = 0.85$ ,  $C_g = 2.86$  and  $C_d = 2.0$ , which are the default values. The vectorial velocity is denoted as  $\vec{v}$ , the turbulent kinetic energy as  $k$ , and the dissipation rate as  $\epsilon$ .  $\mu_t$  is the turbulent (eddy) viscosity. Note that the aforementioned assumption of equal diffusion rates is considered appropriate due to the presence of high-velocity inlet nozzles, as depicted in Figure 6. Based on the high-velocity nozzle geometry, a Reynolds number of 6600 is ensured even for the “lowest velocity case” (i.e., Case 2 with an ER = 0.90 and 35 vol%  $\text{O}_2$  in the oxidator) (Based on a cross-section of the high-velocity nozzle of  $4.5 \cdot 10^{-6} \text{ m}^2$ , a hydraulic diameter of 2 mm and an inlet velocity of 48 m/s). Since the nozzle jets burst when entering the reaction zone, enough turbulence is certainly present to ensure the validity of the non-premixed combustion model.

In this study, the application of a skeletal reaction mechanism in an SFM framework is presented, and the results are compared to those from an experimental furnace. These trials made it possible to determine whether the SFM-based non-premixed combustion model could be modified to handle PSS combustion, also under oxygen-enhanced conditions. The reaction mechanism employed in this study, the so-called heptane42.che, was derived for the combustion of n-heptane by Bui-Pharm et al. [37].

Within this SFM framework, the goal is to investigate the effect of varying water content in the PSS, which according to the water–gas shift reaction Equation (13) is expected to yield higher CO<sub>2</sub> and H<sub>2</sub> concentrations.



The heterogeneous shift reaction in Equation (14), on the other hand, might cause higher CO concentrations, depending on which effect is more dominant. Within this study, one goal is to investigate this effect or, more specifically, whether these effects are relevant at all.



Another aspect is the implementation of the effect that the limestone (mainly CaCO<sub>3</sub>) additive has on the resulting species concentrations in the furnace and how it can be implemented in the model. According to reaction Equation (15), higher CO<sub>2</sub> contents in the flue gas are to be expected.



In total, 12 CFD cases with two different equivalence ratios (ER as defined according to Equation (16)) and oxygen-enhancement levels are described and compared. According to this definition, a sub-stoichiometric case has an ER below 1, while the ER is higher than 1 in a combustion case. The term “oxidator” refers to (oxygen-enriched) air, which is considered to be solely a mixture of oxygen and nitrogen for reasons of simplicity.

$$\begin{aligned} \text{ER} &= \frac{\text{actual fuel–air ratio}}{\text{stoichiometric fuel–air ratio}} \\ &= \frac{\text{amount of oxidator available}}{\text{stoich. required amount of oxidator}} \end{aligned} \quad (16)$$

The simulations in this study are mainly divided in two cases:

- Case 1 deals with the over-stoichiometric combustion of PSS at an ER = 1.2, which should guarantee complete burnout of the fuel.
- Case 2 considers oxygen-enhanced, but sub-stoichiometric combustion (slight gasification) of PSS.

The latter case is interesting for applications where the flue gas might be used as a product gas, e.g., as supplementary fuel in process engineering. The energy required for the gasification is provided by the PSS itself, which makes the process efficient. Because the LHV of PSS is low, this would require oxygen enhancement since the necessary temperature levels would otherwise not be reached.

A main feature of this study is that the CFD results were compared with experimental data. Such data points are often difficult to obtain since sewage sludge as a fuel has certain undesirable properties (formation of agglomerates), which can make it complicated to obtain accurate measurements.

#### 2.3.4. Devolatilization Modelling

In this study, a fully detailed investigation and description of the devolatilization effects is not considered necessary because of the reasons outlined in Section 2.3.2. Instead, a simple single-step kinetic rate model, which was developed by Badzioch et al. [38], was applied. The devolatilization was modelled as linearly dependent on the amount of fuel remaining in the particle. A pre-exponential factor of  $A=312.000 \text{ s}^{-1}$  and an activation energy of  $E_a = 7.4 \cdot 10^7 \text{ J/kmol}$  was used for all simulation cases. This represents values for lignite [39], which was considered similar enough to PSS regarding its composition (see Table 1) and anticipated behaviour in an entrained flow furnace. The starting temperature for devolatilization had to be lowered to 100 °C since the drying and evaporation effect of

the water content is also included in the surrogate fuel approach. However, the starting value for devolatilization had minimal impact on the final results. This simplification is justified due to the small particle sizes and rapid particle heating rates in the order of multiple  $10^5$  K/s, which occur due to the hot flue gas recirculation and high wall temperatures near the burner. These circumstances promote rapid devolatilization and ignition of the PSS, which was also observed during the experiments.

### 2.3.5. Radiation

The discrete ordinates model [40] together with a Weighted Sum of Gray Gases Model (WSGGM) [41] with standard coefficients from Smith et al. [42] were used to account for the gas and black-body radiation. An angular discretization of  $3 \times 3$  was chosen for each octant. This model also allowed us to consider the necessary particle-radiation interaction, which further supports high heating rates. The particle emissivity and absorption coefficients were both assumed to be 0.9.

### 2.3.6. Boundary Conditions

As mentioned, the skeletal reaction mechanism `heptane42.che` was developed for n-heptane combustion. Since the sewage sludge volatiles are not pure heptane, a surrogate fuel composition needed to be found. To represent the original PSS accurately, the surrogate fuel ideally needs to have:

- Correct H<sub>2</sub>O and N<sub>2</sub> mass fractions to consider water content and fuel nitrogen.
- A H/C and O/C ratio close to that of the original PSS, as given in Table 2.
- The same stoichiometric oxygen demand as is required by the original PSS to obtain consistent inlet velocities (momentum flux) at the burner.
- Volatile and char mass fractions of the particles that match the proximate analysis, otherwise particle track calculations would be based on erroneous mass properties.
- The same adjusted LHV as compared to the original PSS.

Ideally, this leads to the definition of particles in CFD that will emit a surrogate fuel with very similar properties (H/C, O/C, volatile and char mass fractions, LHV...) as compared to the original fuel particles. However, not all of the requirements can be perfectly met at the same time, and the system of equations is complex. Therefore, an *Excel* solver tool was created to obtain appropriate surrogate fuel compositions. These can be used with the skeletal reaction mechanism to pre-calculate the chemistry. The solving procedure in *Excel* ensures that the surrogate fuel fulfils the requirements listed above as closely as possible. The following steps and conditions were followed when applying this tool:

(1) Calculate the N<sub>2</sub> and H<sub>2</sub>O mole fractions for the surrogate fuel from the original PSS water content and nitrogen mass fractions. This way, the water content is directly represented by the H<sub>2</sub>O mole fraction in the surrogate fuel. Additional H<sub>2</sub>O (steam) is formed due to the combustion of volatile species. In the same way, the correct amount of fuel-nitrogen will enter the domain in addition to the N<sub>2</sub> that comes in through the oxidator inlets.

(2) Solving for the combustible surrogate composition: Automatically alternate the CO, CO<sub>2</sub>, H<sub>2</sub>, C<sub>3</sub>H<sub>6</sub> and C<sub>7</sub>H<sub>16</sub> mole fractions of the surrogate fuel using a non-linear solving method. This should be done in a way (auxiliary conditions) that

- All considered surrogate components are present.
- The H/C and O/C errors are minimized. Therefore, the atomic composition of the surrogate fuel is close to that of the original PSS.
- The stoichiometric air demand error is minimized, which leads to the same inlet momentum flux from the burner.
- The original and the surrogate fuel emitting particle have the same ash mass fraction and LHV.

The surrogate fuel was adjusted to generate the correct enthalpy flow while maintaining a volatile mass fraction of, e.g., 0.51 and a combustible mass fraction of, e.g., 0.041 for the case with 10% water content. In this way, it is possible to mimic the char burnout, a heterogeneous surface reaction, albeit by the single surrogate fuel compositions. The char burnout is described by a kinetics/diffusion limited approach with a rate constant of  $5 \times 10^{-12}$ , a pre-exponential factor of 6.7 and an activation energy of  $E_a = 1.138 \cdot 10^8$  J/kmol. Using these settings, a particle in CFD will have an equivalent ash-mass fraction to the original PSS. These considerations make it possible to accurately represent the occurring slag amount, and thus provide the necessary basis for further research and model improvements.

### 2.3.7. Implementation of the Limestone Effect

The calcination reaction Equation (15) shows the idealized decomposition of limestone ( $\text{CaCO}_3$ ) into  $\text{CO}_2$  and  $\text{CaO}$ . For every mole of limestone, one mole of  $\text{CO}_2$  can be expected due to this reaction, which is highly endothermic.

Given a specific mass flow of  $\text{CaCO}_3$  as in our case, where it is added to PSS in a fixed ratio, an additional amount of  $\text{CO}_2$  is to be expected in the flue gas of the reactor. The SFM framework in Fluent only allows one mixture fraction. Therefore, the only way to implement the calcination effect on the gas phase composition is to consider additional  $\text{CO}_2$  in the surrogate fuel composition, as shown in Table 3. This is clearly a highly simplified concept to capture the effect which the limestone might have on the equilibrium concentrations. It is not a detailed simulation of entrained flow calcination.

The heat of reaction of the calcination reaction is incorporated into the model by means of an apparent particle specific heat curve  $c_p$ , which has a peak in the range where the reaction occurs. Due to the mass balance of the calcination reaction, the solid limestone particle is expected to lose 43.96% of its mass during its transformation into  $\text{CaO}$ . An additional injection of limestone particles was created to account for the additional  $\text{CaCO}_3$  mass flow. The additional particles have a volatile fraction of 43.96%. Therefore, the solid matter (DPM) mass balance is satisfied.

Table 3 summarizes the calculated surrogate compositions for different amounts of limestone additive. Table 4 displays surrogate compositions for varying water contents.

**Table 3.** Surrogate fuel compositions for all basicities (10% water content).

Heptane42 Component	Mole Fraction Surrogate Fuel No Additive	Mole Fraction Surrogate Fuel 10% $\text{CaCO}_3$	Mole Fraction Surrogate Fuel 20% $\text{CaCO}_3$
$\text{H}_2\text{O}$	0.378	0.354	0.333
$\text{H}_2$	0.030	0.028	0.026
$\text{CO}$	0.050	0.047	0.044
$\text{CO}_2$	0.300	0.345	0.384
$\text{C}_3\text{H}_6$	0.030	0.028	0.026
$\text{C}_7\text{H}_{16}$	0.121	0.114	0.107
$\text{N}_2$	0.090	0.085	0.080

**Table 4.** Surrogate fuel compositions for varying water contents (20% CaCO<sub>3</sub> added).

Heptane42 Component	Mole Fraction Surrogate Fuel 10% H <sub>2</sub> O(ar)	Mole Fraction Surrogate Fuel 15% H <sub>2</sub> O	Mole Fraction Surrogate Fuel 20% H <sub>2</sub> O
H <sub>2</sub> O	0.333	0.434	0.514
H <sub>2</sub>	0.026	0.027	0.027
CO	0.044	0.045	0.045
CO <sub>2</sub>	0.384	0.317	0.265
C <sub>3</sub> H <sub>6</sub>	0.026	0.027	0.027
C <sub>7</sub> H <sub>16</sub>	0.107	0.085	0.068
N <sub>2</sub>	0.080	0.065	0.054

The mass flow boundary conditions were set according to Table 5, which shows all ER and oxygen-enhancement settings used in the simulations. An ER below one relates to a fuel-rich process, whereas an ER higher than one indicates fuel-lean (complete) combustion. Note that the values in Table 5 represent one-third of the experimental values since only one-third of the geometry needed to be meshed. All flows enter the computational domain with a set temperature of 27 °C.

**Table 5.** Flow boundary conditions for the CFD models in kg/h, these values represent a third of the experimental values since only a third of the domain was modelled.

<b>Case 1</b>	ER = 1.2	ER = 1.2	ER = 1.2
<b>Limestone additive variations</b>	21vol% O <sub>2</sub> No additive	21vol% O <sub>2</sub> 10% CaCO <sub>3</sub>	21vol% O <sub>2</sub> 20% CaCO <sub>3</sub>
Sewage sludge	1.00	1.00	1.00
Limestone	-	0.10	0.20
Feed air	0.30	0.30	0.30
Annular pipe	1.56	1.56	1.56
High-velocity nozzle	1.80	1.80	1.80
<b>Case 2</b>	ER = 0.9	ER = 0.9	ER = 0.9
<b>Limestone additive variations</b>	35vol% O <sub>2</sub> No additive	35vol% O <sub>2</sub> 10% CaCO <sub>3</sub>	35vol% O <sub>2</sub> 10% CaCO <sub>3</sub>
Sewage sludge	1.00	1.00	1.00
Limestone	-	0.10	0.20
Feed air	0.30	0.30	0.30
Annular pipe	0.45	0.45	0.45
High-velocity nozzle	0.90	0.90	0.90
<b>Case 1</b>	ER = 1.2	ER = 1.2	ER = 1.2
<b>Water content variations</b>	21vol% O <sub>2</sub> 10% H <sub>2</sub> O	21vol% O <sub>2</sub> 15% H <sub>2</sub> O	21vol% O <sub>2</sub> 20% H <sub>2</sub> O
Sewage sludge	1.00	1.00	1.00
Limestone	0.20	0.20	0.20
Feed air	0.30	0.30	0.30
Annular pipe	1.56	1.35	1.15
High-velocity nozzle	1.80	1.80	1.80
<b>Case 2</b>	ER = 0.9	ER = 0.9	ER = 0.9
<b>Water content variations</b>	35vol% O <sub>2</sub> 10% H <sub>2</sub> O	35vol% O <sub>2</sub> 15% H <sub>2</sub> O	35vol% O <sub>2</sub> 20% H <sub>2</sub> O
Sewage sludge	1.00	1.00	1.00
Limestone	0.20	0.20	0.20
Feed air	0.30	0.30	0.30
Annular pipe	0.14	0.05	0.25
High-velocity nozzle	1.19	1.19	0.90

The inner reaction chamber walls with a diameter of 200 mm were set to maintain a constant temperature of 1300 °C since they were electrically heated and controlled during the experiment. An emissivity of 0.9 was assumed for all walls due to the ash deposits. The thermocouple emissivity is set to 0.45 in all simulation models.

### 2.3.8. Solution Procedure and Methods

To solve a case numerically, the following steps were taken to achieve rapid convergence:

1. Solve the oxidator flow only while considering the heated furnace walls until convergence is achieved (turbulent flow field).
2. Add DPM particle tracking without considering the chemical reactions.
3. Include the chemical reactions by activation of the transport equations for the mixture fraction (Equation (11)) and mixture fraction variance (Equation (12)).

Convergence was assessed according to residuals falling below  $10^{-6}$  for the energy, mixture fraction, mixture fraction variance and radiation and below  $10^{-3}$  for the continuity, momentum and turbulence. In addition to the residuals, the monitoring of temperatures, velocities and concentrations at various points in the domain over the iteration count was employed to assess convergence. Pressure velocity coupling was achieved by means of the SIMPLE (Semi Implicit Method for Pressure Linked Equations) algorithm. PRESTO was used for the pressure term discretization. Momentum, energy, turbulence and species-related transport equations were discretized using second-order upwind schemes. For radiation, a first-order upwind scheme was considered to be sufficient.

On a hardware setup with a 12-core CPU and 64 GB RAM, a converged solution (residuals, steady monitors of physical quantities such as temperatures) can be achieved within 2 h of computation time (medium mesh), including all particle track calculations, which comprise a significant proportion of the simulation effort. The advantage over conventional species transport approaches increases with higher cell counts since fewer transport equations (depending on the number of species in an EDM or EDC model) require solving. In this way, complex geometries can be studied in research and development without the need for high-performance computing clusters while still considering detailed chemistry.

## 3. Results and Discussion

In this section, the major results are presented and discussed. Contour plots and data from temperature and species concentration measurements serve as a basis for the evaluation of the investigated CFD modelling approach.

### 3.1. Particle Conversion and Temperatures

Figure 9a shows the resulting temperature field for the SFM model simulation of Case 1, considering an ER of 1.2 and 21vol% O<sub>2</sub> in the oxidator. No additive is used and the water content is as received. From the top, cold oxidator gas enters the domain in distinct jets. Some time is required to mix with the hot flue gases close to the burner inlet. During mixing with the hot gases, the centrally injected particles heat up rapidly. Based on particle volatile mass fractions, Figure 9b indicates that the process of devolatilization happens almost instantly. As soon as the particles mix with the hot gas phase, they lose mass very fast (“flash-devolatilization”). Therefore, the resulting flame is almost exclusively a result of gas-phase reactions. As pointed out above, this is a consequence of the small particle sizes, high heating rates and the high temperature level in the drop tube furnace. Figure 9c displays the particle Biot number, which does not exceed 0.04 even for the largest considered particles. This confirms the assumption of thermally thin particles. Note that for visibility purposes, the particle tracks are not displayed until termination but only for a limited number of particle time steps. Otherwise, the entire visible domain would be filled with particles.



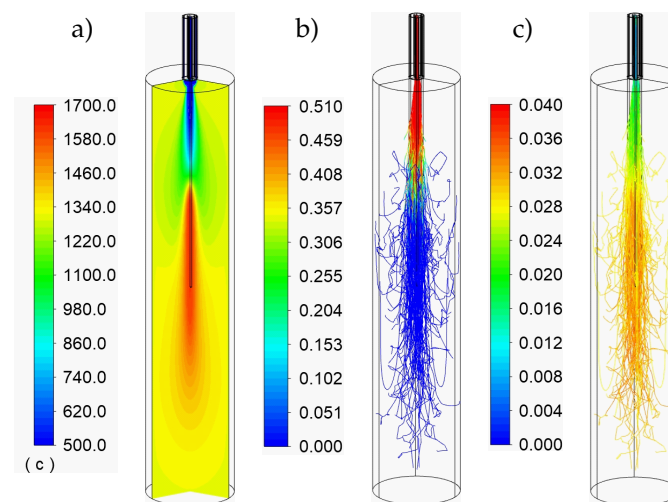


**Figure 9.** Particle conversion-(a) Temperature field for Case 1, no additive, 10% water content (b) Particle volatile mass fraction (c) Particle biot number as defined in Equation (9).

During the experiment, it was possible to measure temperatures in the furnace by means of the vertically adjustable thermocouple (Figure 4). For this case (PSS as received, no additives), a comparison with the simulated values is given in Figure 10. This graphic shows measured (crosses) and simulated (lines) temperatures in °C up to a distance of 0.4 m from the burner inlet. It can be argued that after an initial slight under-prediction of the temperatures, the model predicts the location of temperature increase and the final temperature levels with good accuracy. In addition to the proposed model, the case was also solved using a conventional CEQ approach. Its results are also indicated in Figure 10 with the dashed line. There is no significant difference between the results, although the CEQ results seem slightly higher.

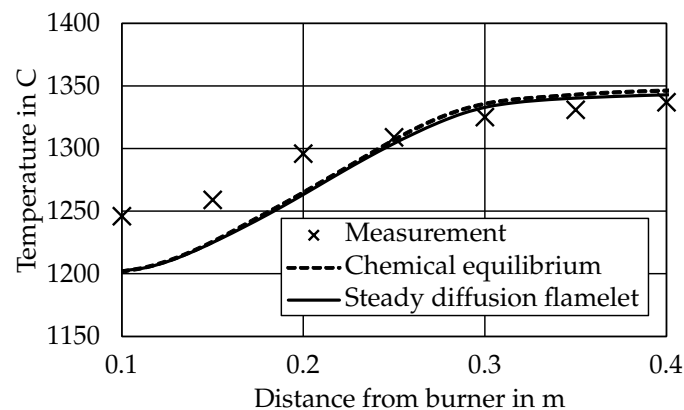


**Figure 10.** Temperature profile for case 1 and comparison with SFM CFD results (PSS as received, no additives).

Another temperature measurement was completed during an experiment with the same ER but using an oxygen-enhanced oxidator with 35vol% O<sub>2</sub>. Due to the lower required amount of oxidator mass flow, higher temperatures and a flame closer to the burner inlet are expected. The data shown in Figure 11, which again displays temperature profiles up to a distance of 0.4 m from the burner inlet, confirms this assumption. Although the SFM-based model predicts a faster temperature increase, it fails to calculate an accurate heat release, leading to unsatisfactory low temperatures 0.25–0.40 m after the burner inlet.

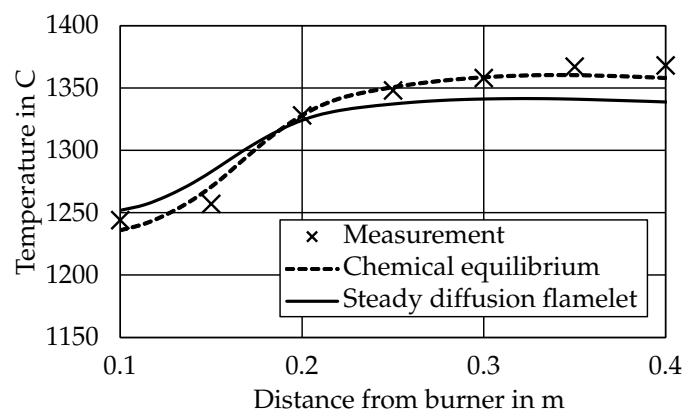


**Figure 11.** Temperature profile with an equivalence ratio as in case 1 but with oxygen enhancement (35vol% O<sub>2</sub>), SFM fails to predict full burnout.

This insufficient burnout was noticed during all simulations of oxygen-enhanced cases. When switching to a conventional chemical equilibrium model (CEQ), which uses the same approach as the model suggested in this study, but under the assumption of chemical equilibrium and not based on a skeletal reaction mechanism, it can be easily shown that the measured temperatures would be easily reached. This is displayed by the dashed line in Figure 11, which fits the measured data very well.

Together with the observation of highly reactive particle behaviour, these results confirm our assumption of gas-phase chemistry as the main factor during the entrained flow combustion of very small PSS particles in this high-temperature process.

### 3.2. Species Concentrations

Considering species concentrations, mainly the effects of water content and limestone additive will be the focus in this section. It was not feasible to determine gas composition profiles experimentally due to heavy slagging during the experiment (closer to the burner). Therefore, the experimental results would have insufficient accuracy. Nevertheless, the main difference between the SFM-based model and a chemical equilibrium approach will be discussed first by means of species concentration profiles.

#### 3.2.1. CEQ vs. SFM Approach

Figure 12 compares the main gas-phase results of the SFM-based model with CEQ model results (Case 1 with no additive, water content 20%). The graphic shows species concentrations (dry-based mole fractions) as axial profiles depending on the distance from the burner inlet. First, it should be noted that the results differ only very slightly, but in some noteworthy details: The CEQ model results show significant peaks in the axial CO<sub>2</sub> species profiles, which is not predicted by the SFM-based results. Furthermore, the CEQ model predicts much higher CO concentrations than the SFM model. This confirms the SFM model's ability to consider slight non-equilibrium effects. It allows for the prediction of a more realistic combustion evolution. The figure shows that both modelling approaches agree on the location of the main reaction zones. The final results both agree very well with experimentally determined data.

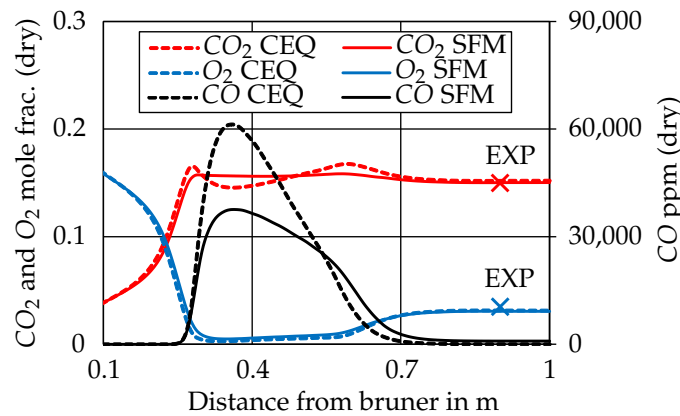


**Figure 12.** Species concentration results for Case 1–10% water content (ar), no additive (profiles through main furnace axis) for both models.

The overall heat release for both models agrees well, unlike in the case where a higher O<sub>2</sub> content in the oxidator gas is used (see Figures 10 vs. 11). For this reason, the following approach is used to assess the results concerning water content and limestone effects:

- Case 1 is evaluated with the surrogate approach using the SFM model as described above with no modifications.
- Case 2 is evaluated with the surrogate approach using the CEQ model.

### 3.2.2. Effect of the Limestone Additive

The simple calcination modelling concept assumes full conversion of the limestone CaCO<sub>3</sub> to CO<sub>2</sub> and CaO according to Equation (15). Therefore, measured and calculated CO<sub>2</sub> species results will be compared in Figure 13. The considered water content in the PSS was 10% (ar). From left to right, rising levels of additive amounts are shown. Starting at the case with no additive, simulation and experiment agree well on a value of around 15% CO<sub>2</sub> based on 3.5% O<sub>2</sub> in the dry flue gas, which is the stoichiometric amount. With the addition of limestone to the fuel, indeed, higher CO<sub>2</sub> concentrations are detected in the experiment, very much to the degree that this simplified model predicts.

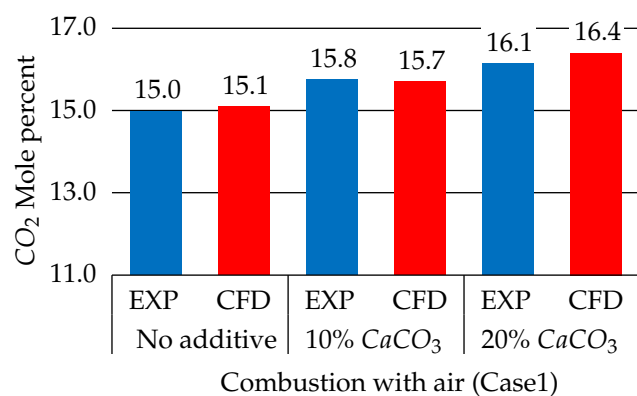


**Figure 13.** Effect of limestone additive on the flue gas concentrations, experimental data is based on 3.5% O<sub>2</sub> in the flue gas (dry).

Figure 14 provides the same comparison of experimental and numerical data for Case 2. Again, CO<sub>2</sub> concentrations clearly rise with more limestone added during the experiment. The values are very well predicted by the numerical results. The “\*” in the CFD results indicates that they were obtained with the CEQ-based model since the burnout at high oxygen-enhancement levels would be otherwise incorrectly predicted. This would result in underestimated CO<sub>2</sub> and overestimated O<sub>2</sub> concentrations in the flue gas.

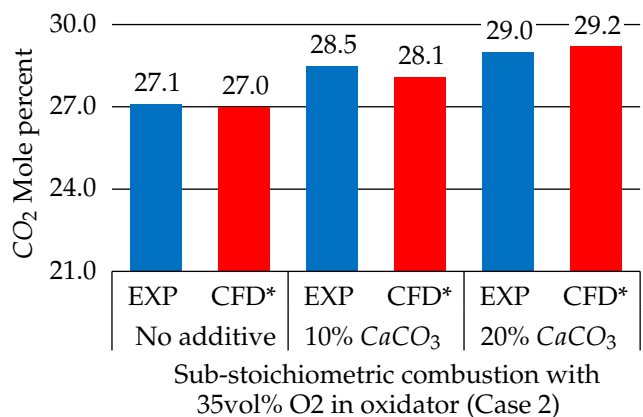


Figure 14. Effect of limestone additive on the flue gas concentrations (dry); “CFD\*” indicates the calculation by the CEQ approach.

3.2.3. Water Content Effects

Case 1 was successfully experimentally investigated at three different levels of water content in the PSS. As described in Section 2.2, the varying water contents were replicated by injection of the according amount of steam into the reactor. All water-content-related cases used PSS with 20% limestone additive. Figure 15 summarizes the main results of these three experiments with increasing water content from left to right. All values are based on 3.5% O<sub>2</sub> in the dry flue gas, which is the stoichiometric amount.

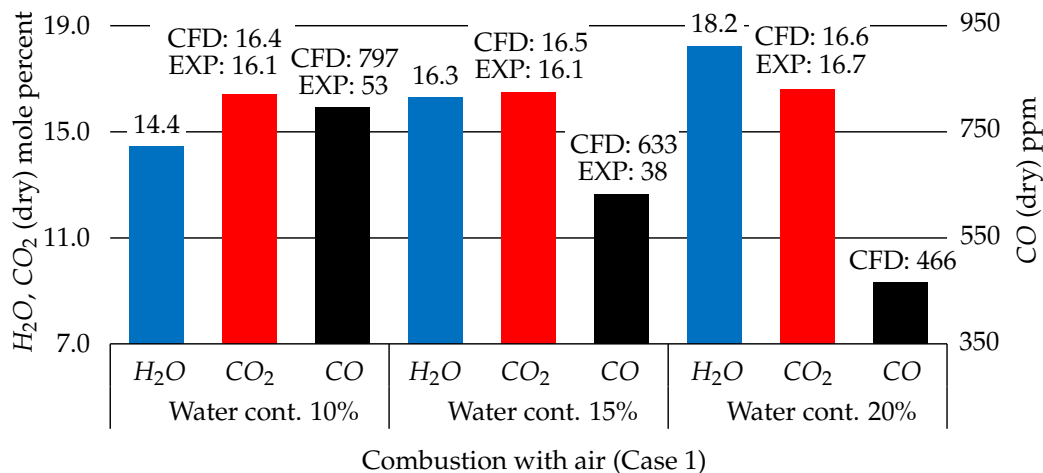
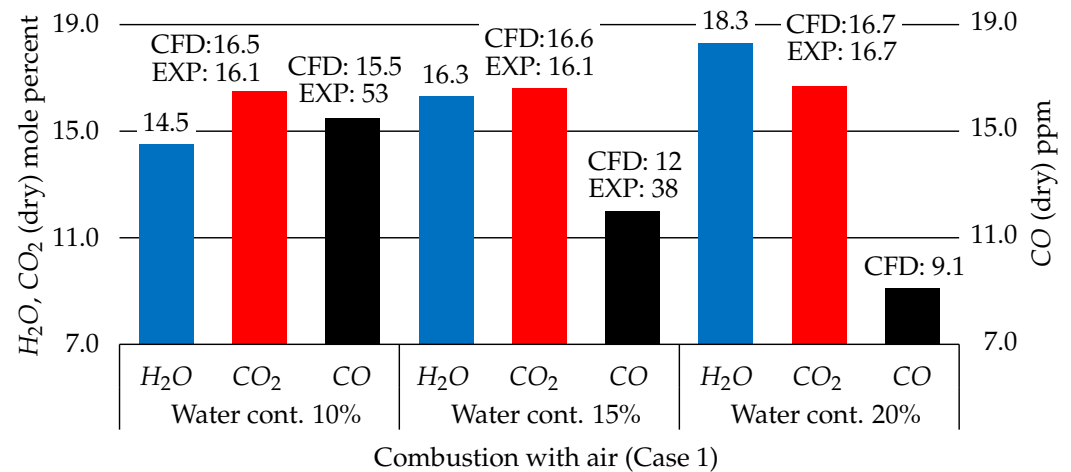


Figure 15. Effect of increased water content on the flue gas concentrations (dry), experimental data are based on 3.5% O<sub>2</sub> in the flue gas (dry).

Starting at 10% water content (PSS as received, 20% limestone, no added steam), a dry concentration of 16.1% of CO<sub>2</sub> was measured while a low CO concentration of 53 ppm was observed. The SFM-based CFD model predicts 16.4% CO<sub>2</sub>, which is very close to the experimental value. The CO fraction, however, was overestimated significantly at 797 ppm. It has to be noted that these are very low values and measurement uncertainties are high. For an increased amount of water in the system, the measured CO<sub>2</sub> value was still at 16.1% while the CO fraction dropped to 38 ppm. The CFD model predicted a slightly increased CO<sub>2</sub> value, while the CO concentration fell to 633 ppm. The highest considered water content of 20% led to measured 16.7% while the CFD model predicted 16.6% and only 466 ppm. CO measurement data were unavailable for this point. Generally, since the SFM-based model considers gas-phase reactions with a detailed mechanism, the shift effect appears in the simulated results. Experimentally, the concentrations also seemed to

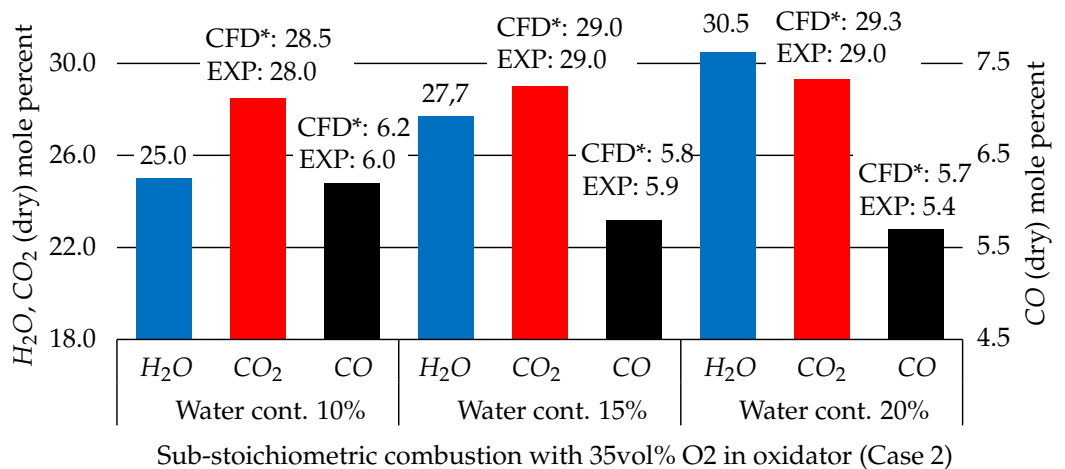
decrease, although uncertainty remains as to what degree the heterogeneous shift reaction influences this result.

Figure 16 additionally shows the case 1 results calculated by the CEQ model. The only significant difference in the equilibrium compositions can be found in the much lower CO concentrations at 15.5 ppm compared to the SFM model. They are below experimental values of 53 ppm for the lowest water content and drop as the fuel humidity rises. In addition to the CO ppm overestimation, the SFM model can accurately predict the equilibrium flue gas concentrations and has the advantage of featuring a validated reaction mechanism.



**Figure 16.** Effect of increased water content on the flue gas concentrations (dry), experimental data are based on 3.5% O<sub>2</sub> in the flue gas (dry), Calculation with CEQ approach.

Figure 17 works in the same way but for the sub-stoichiometric combustion (Case 2) with 35vol% O<sub>2</sub> in the oxidator. Here, calculated and experimentally determined values are in close accordance for all cases. At sub-stoichiometric conditions, the CO values are also much more significant. Indeed, lower CO values were experimentally observed at these conditions when higher water contents were considered. This decrease in CO, on the other hand, is still not very pronounced. The CFD model also predicted lower CO mole fractions with rising water content.



**Figure 17.** Effect of increased water content on flue gas concentrations (dry); "CFD\*" indicates the calculation by the CEQ approach.

In Figure 18, the results of case 2 as calculated by the SFM model are shown. Compared to the CEQ results in Figure 17, the SFM model predicts significantly lower CO<sub>2</sub> and higher CO concentrations. This is due to the inaccurate burnout, which can also be observed in

the temperature profiles (Figure 11). The SFM-based model further predicts residual  $O_2$  in the flue gas composition at these conditions, which contradicts measurement data. At the location where the gas concentrations were measured, chemical equilibrium is reached, and the CEQ model predicts the flue gas composition much better.

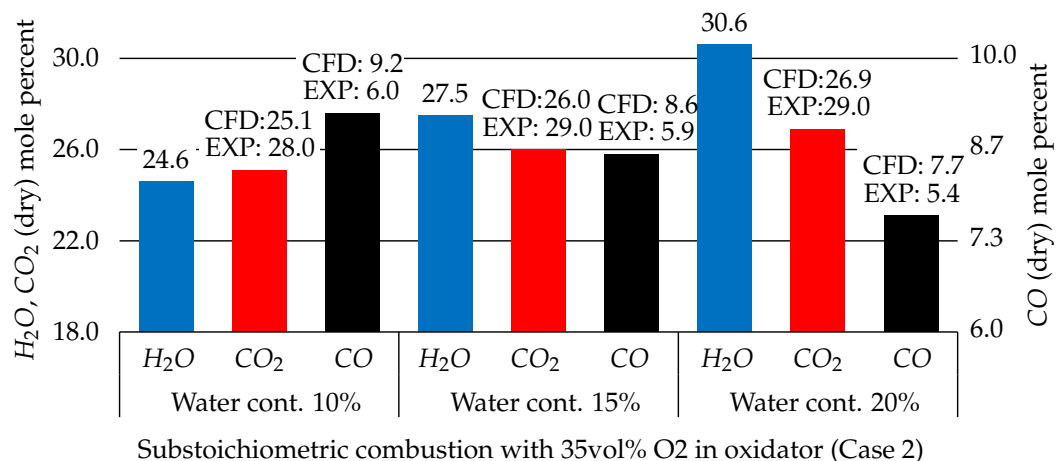


**Figure 18.** Effect of increased water content on the flue gas concentrations (dry); Calculation by the SFM approach.

On the basis of these results, we argue that the effect of varying water contents is measurable and also depicted by the surrogate-based CFD model. Still, it is not very pronounced, and practical relevance is limited, especially with the variety of other uncertainties (PSS chemical composition, dosing accuracy etc.) in mind.

Overall, the effect of limestone is much more pronounced than the effect of varying water content and should therefore be given more attention for our purpose.

#### 4. Conclusions and Outlook

The numerically inexpensive CFD model yields highly satisfactory results and works as intended for the entrained combustion and gasification cases in air. The SFM model results show that the surrogate fuel modelling approach is valid, even though the skeletal reaction mechanism is based on heptane combustion. In this way, the implemented effect of long-chained hydrocarbon reaction kinetics leads to a realistic combustion evolution and correct equilibrium results, which were confirmed experimentally.

However, at higher oxygen enhancement levels (e.g., 35 vol%  $O_2$  in the oxidator and more), one must exercise caution since the heptane42.che mechanism predicted an incorrect burnout and heat release. For most cases, the SFM model with heptane42.che is suitable as a method to predict the combustion and gasification of PSS in a computationally inexpensive manner. It works well at all additive and water content settings and with all equivalence ratios. Nevertheless, if a case with high oxygen-enhancement levels is considered, we recommend using the conventional CEQ model with the surrogate approach. This enables a complete release of the energy content (LHV) in PSS.

The surrogate approach leads to a model that can be rapidly solved. It bears great potential for application in full-scale industry research and development areas. Feedback on design changes needs to be rapidly post-processed from CFD models and with the necessary levels of prediction accuracy. Complex geometries, which demand high cell counts, are the norm in these fields. On the other hand, high-performance computing clusters are seldom available, so the models need to run on conventional hardware.


Concerning the impact of varying water content in the PSS, the model predicted less CO ppm (combustion) and mole fractions (sub-stoichiometric combustion) for increasing water content. However, changes in the flue gas compositions were minor, which was also confirmed by the experiment. Therefore, a significant water–gas shift at realistic operating conditions cannot be expected.

The addition of limestone additive was implemented into the SFM model's surrogate approach under the assumption of complete calcination of the material. When using higher amounts of added limestone, the predicted increase in CO<sub>2</sub> species could be experimentally verified.

Since the models allow for reasonably accurate predictions of the atmospheric conditions (gas species concentrations and temperatures) in an entrained flow PSS combustion/gasification reactor, these approaches can serve as a basis for more detailed particle kinetic models (e.g., models that can be used to predict phosphorus yield) in the near future. Since all relevant DPM particle properties, such as particle densities and sizes, remain unchanged by the SFM-based modelling approach, further particle physics investigations (slag collection, carry-over, etc.) can be accurately predicted in upcoming model updates.

**Author Contributions:** Conceptualization, B.O. and C.S.; methodology, B.O. and C.S.; software, B.O.; validation, B.O., C.S., R.P. and H.G.; formal analysis, B.O. and R.P.; investigation, B.O.; resources, C.H.; data curation, B.O., C.S. and H.S.; writing—original draft preparation, B.O.; writing—review and editing, B.O., C.S., R.P., H.G. and C.H.; visualization, B.O.; supervision, C.H.; project administration, C.H.; funding acquisition, C.H. All authors have read and agreed to the published version of the manuscript.

**Data Availability Statement:** The data presented in this study are available on request from the corresponding author.

**Funding:** This project has received funding from the European Union's Horizon 2020 research and innovation programme under grant agreement No 958267. 

**Conflicts of Interest:** The authors declare that they have no known competing financial interests or personal relationships that could have appeared to influence the work reported in this paper.

**Disclaimer:** This publication reflects only the authors' views, and the European Health and Digital Executive Agency (HaDEA) and the European Commission are not responsible for any use that may be made of the information it contains.

## Abbreviations

The following abbreviations are used in this manuscript:

CEQ	Chemical equilibrium model
CFD	Computational fluid dynamics
DIA	Dynamic image analysis
DPM	Discrete phase model
EDM	Eddy dissipation model
EDC	Eddy dissipation concept
ER	Equivalence ratio
LCV	Lower calorific value
MFC	Mass flow controller
PSD	Particle size distribution
PSS	Pulverized sewage sludge
SEM	Scanning electron microscopy
RRSB	Rosin–Rammler–Sperling–Bennett (particle size distribution)
SFM	Steady diffusion flamelet
TC	Thermocouple
TGA	Thermogravimetric analysis
UDF	User-defined function
ar	As received
ppm	Parts per million
<i>Re</i>	Reynolds number
<i>Bi</i>	Biot number
<i>u<sub>p</sub></i>	Particle velocity
<i>t</i>	Time

$F_D$	Drag force
$u$	Gas phase velocity
$g$	Gravity
$\rho_p$	Particle density
$\rho$	Gas phase density
$\mu$	Molecular viscosity of the gas phase
$d_p$	Particle diameter
$c_D$	Drag coefficient
$m_p$	Particle mass
$c_p$	Particle specific heat
$T_p$	Particle temperature
$V_p$	Particle volume
$A_p$	Particle surface area
$\lambda_p$	Particle thermal conductivity

## References

- Chanaka Udayanga, W.D.; Veksha, A.; Giannis, A.; Lisak, G.; Chang, V.W.C.; Lim, T.T. Fate and distribution of heavy metals during thermal processing of sewage sludge. *Fuel* **2018**, *226*, 721–744. [\[CrossRef\]](#)
- Roy, M.M.; Dutta, A.; Corscadden, K.; Havard, P.; Dickie, L. Review of biosolids management options and co-incineration of a biosolid-derived fuel. *Waste Manag.* **2011**, *31*, 2228–2235. [\[CrossRef\]](#) [\[PubMed\]](#)
- Namkung, H.; Lee, Y.J.; Park, J.H.; Song, G.S.; Choi, J.W.; Choi, Y.C.; Park, S.J.; Kim, J.G. Blending effect of sewage sludge and woody biomass into coal on combustion and ash agglomeration behavior. *Fuel* **2018**, *225*, 266–276. [\[CrossRef\]](#)
- Stelmach, S.; Wasielewski, R. Co-combustion of dried sewage sludge and coal in a pulverized coal boiler. *J. Mater. Cycles Waste Manag.* **2008**, *10*, 110–115. [\[CrossRef\]](#)
- Pellegrini, M.; Saccani, C.; Bianchini, A.; Bonfiglioli, L. Sewage sludge management in Europe: A critical analysis of data quality. *Int. J. Environ. Waste Manag.* **2016**, *18*, 226. [\[CrossRef\]](#)
- Le Quan, M.; Kamyab, H.; Yuzir, A.; Ashokkumar, V.; Hosseini, S.E.; Balasubramanian, B.; Kirpichnikova, I. Review of the application of gasification and combustion technology and waste-to-energy technologies in sewage sludge treatment. *Fuel* **2022**, *316*, 123199. [\[CrossRef\]](#)
- Atienza-Martínez, M.; Gea, G.; Arauzo, J.; Kersten, S.R.; Kootstra, A.M.J. Phosphorus recovery from sewage sludge char ash. *Biomass Bioenergy* **2014**, *65*, 42–50. [\[CrossRef\]](#)
- Schoumans, O.F.; Bouraoui, F.; Kabbe, C.; Oenema, O.; van Dijk, K.C. Phosphorus management in Europe in a changing world. *Ambio* **2015**, *44* (Suppl. S2), S180–S192. [\[CrossRef\]](#)
- Wang, Y.; Yan, L. CFD based combustion model for sewage sludge gasification in a fluidized bed. *Front. Chem. Eng. China* **2009**, *3*, 138–145. [\[CrossRef\]](#)
- Yani, S.; Gao, X.; Wu, H. Emission of Inorganic PM 10 from the Combustion of Torrefied Biomass under Pulverized-Fuel Conditions. *Energy Fuels* **2015**, *29*, 800–807. [\[CrossRef\]](#)
- Feng, C.; Huang, J.; Yang, C.; Li, C.; Luo, X.; Gao, X.; Qiao, Y. Smouldering combustion of sewage sludge: Volumetric scale-up, product characterization, and economic analysis. *Fuel* **2021**, *305*, 121485. [\[CrossRef\]](#)
- Fletcher, D.F.; Haynes, B.S.; Christo, F.C.; Joseph, S.D. A CFD based combustion model of an entrained flow biomass gasifier. *Appl. Math. Model.* **2000**, *24*, 165–182. [\[CrossRef\]](#)
- Lin, H.; Ma, X. Simulation of co-incineration of sewage sludge with municipal solid waste in a grate furnace incinerator. *Waste Manag.* **2012**, *32*, 561–567. [\[CrossRef\]](#) [\[PubMed\]](#)
- Žnidarčič, A.; Seljak, T.; Katrašnik, T. Surrogate model for improved simulations of small-scale sludge incineration plants. *Fuel* **2020**, *280*, 118422. [\[CrossRef\]](#)
- Žnidarčič, A.; Katrašnik, T.; Zsély, I.G.; Nagy, T.; Seljak, T. Sewage sludge combustion model with reduced chemical kinetics mechanisms. *Energy Convers. Manag.* **2021**, *236*, 114073. [\[CrossRef\]](#)
- Buchmayr, M.; Gruber, J.; Hargassner, M.; Hochenauer, C. A computationally inexpensive CFD approach for small-scale biomass burners equipped with enhanced air staging. *Energy Convers. Manag.* **2016**, *115*, 32–42. [\[CrossRef\]](#)
- Buchmayr, M.; Gruber, J.; Hargassner, M.; Hochenauer, C. Performance analysis of a steady flamelet model for the use in small-scale biomass combustion under extreme air-staged conditions. *J. Energy Inst.* **2018**, *91*, 534–548. [\[CrossRef\]](#)
- Buchmayr, M.; Gruber, J.; Hargassner, M.; Hochenauer, C. Spatially resolved chemical species concentrations above the fuel bed of a small grate-fired wood-chip boiler. *Biomass Bioenergy* **2016**, *95*, 146–156. [\[CrossRef\]](#)
- Watanabe, J.; Yamamoto, K. Flamelet model for pulverized coal combustion. *Proc. Combust. Inst.* **2015**, *35*, 2315–2322. [\[CrossRef\]](#)
- Wen, X.; Fan, J. Flamelet modeling of laminar pulverized coal combustion with different particle sizes. *Adv. Powder Technol.* **2019**, *30*, 2964–2979. [\[CrossRef\]](#)
- Mularski, J.; Modliński, N. Entrained flow coal gasification process simulation with the emphasis on empirical devolatilization models optimization procedure. *Appl. Therm. Eng.* **2020**, *175*, 115401. [\[CrossRef\]](#)



22. Mularski, J.; Pawlak-Kruczek, H.; Modlinski, N. A review of recent studies of the CFD modelling of coal gasification in entrained flow gasifiers, covering devolatilization, gas-phase reactions, surface reactions, models and kinetics. *Fuel* **2020**, *271*, 117620. [[CrossRef](#)]
23. Zhu, X.; Zhao, L.; Fu, F.; Yang, Z.; Li, F.; Yuan, W.; Zhou, M.; Fang, W.; Zhen, G.; Lu, X.; et al. Pyrolysis of pre-dried dewatered sewage sludge under different heating rates: Characteristics and kinetics study. *Fuel* **2019**, *255*, 115591. [[CrossRef](#)]
24. Mehrabian, R.; Scharler, R.; Obernberger, I. Effects of pyrolysis conditions on the heating rate in biomass particles and applicability of TGA kinetic parameters in particle thermal conversion modelling. *Fuel* **2012**, *93*, 567–575. [[CrossRef](#)]
25. Kobayashi, H.; Howard, J.B.; Sarofim, A.F. Coal devolatilization at high temperatures. *Symp. Int. Combust.* **1977**, *16*, 411–425. [[CrossRef](#)]
26. Schmid, M.; Beirow, M.; Schweitzer, D.; Waizmann, G.; Spörl, R.; Scheffknecht, G. Product gas composition for steam-oxygen fluidized bed gasification of dried sewage sludge, straw pellets and wood pellets and the influence of limestone as bed material. *Biomass Bioenergy* **2018**, *117*, 71–77. [[CrossRef](#)]
27. Al-Abbas, A.H.; Naser, J.; Dodds, D. CFD modelling of air-fired and oxy-fuel combustion in a large-scale furnace at Loy Yang A brown coal power station. *Fuel* **2012**, *102*, 646–665. [[CrossRef](#)]
28. Steibel, M.; Halama, S.; Geißler, A.; Spliethoff, H. Gasification kinetics of a bituminous coal at elevated pressures: Entrained flow experiments and numerical simulations. *Fuel* **2017**, *196*, 210–216. [[CrossRef](#)]
29. Mu, L.; Wang, S.; Zhai, Z.; Shang, Y.; Zhao, C.; Zhao, L.; Yin, H. Unsteady CFD simulation on ash particle deposition and removal characteristics in tube banks: Focusing on particle diameter, flow velocity, and temperature. *J. Energy Inst.* **2020**, *93*, 1481–1494. [[CrossRef](#)]
30. Menter, F.R. Zonal Two Equation k- $\omega$  Turbulence Models For Aerodynamic Flows. In Proceedings of the AIAA 24th Fluid Dynamics Conference, Orlando, FL, USA, 6–9 July 1993. [[CrossRef](#)]
31. Christ, D. *The Effect of Char Kinetics on the Combustion of Pulverized Coal under Oxyfuel Conditions*; Diss. RWTH Aachen University: Aachen, Germany, 2013; ISBN 13:978-3-86844-559-6.
32. Haider, A.; Levenspiel, O. Drag coefficient and Terminal Velocity of Spherical and Nonspherical Particles. *Powder Technol.* **1988**, *58*, 63–70. [[CrossRef](#)]
33. Ranz, W.M. Evaporation from drops. *Chem. Eng. Prog.* **1952**, *48*, 141–146.
34. Werther, J.; Ogada, T. Sewage sludge combustion. *Prog. Energy Combust. Sci.* **1999**, *25*, 55–116. [[CrossRef](#)]
35. Werther, J.; Ogada, T. Combustion characteristics of wet sludge in a fluidized bed. *Fuel* **1996**, *5*, 617–626. [[CrossRef](#)]
36. Cui, H.; Ninomiya, Y.; Masui, M.; Mizukoshi, H.; Sakano, T.; Kanaoka, C. Fundamental Behaviors in Combustion of Raw Sewage Sludge. *Energy Fuels* **2006**, *20*, 77–83. [[CrossRef](#)]
37. Bui-Pham, M.; Seshadri, K. Comparison between Experimental Measurements and Numerical Calculations of the Structure of Heptane-Air Diffusion Flames. *Combust. Sci. Technol.* **1991**, *74*, 293–310. [[CrossRef](#)]
38. Badzioch, S.; Hawksley, P.G.W. Kinetics of Thermal Decomposition of Pulverized Coal Particles. *Ind. Eng. Chem. Process. Des. Dev.* **1970**, *9*, 521–530. [[CrossRef](#)]
39. *ANSYS Fluent Theory Guide, Release 2020 R2*; ANSYS, Inc.: Canonsburg, PA, USA, 2020.
40. Raithby, G.D.; Chui, E.H. A Finite-Volume Method for Predicting a Radiant Heat Transfer in Enclosures with Participating Media. *J. Heat. Transf.* **1990**, *112*, 415–423. [[CrossRef](#)]
41. Hottel, H.C.; Cohen, E.S. *Radiative Transfer*; McGraw-Hill Book Company: New York, NY, USA, 1967. [[CrossRef](#)]
42. Smith, T.F.; Shen, Z.F.; Friedman, J.N. Evaluation of Coefficients for the Weighted Sum of Gray Gases Mode. *J. Heat Transf.* **1982**, *104*, 602–608. [[CrossRef](#)]

**Disclaimer/Publisher’s Note:** The statements, opinions and data contained in all publications are solely those of the individual author(s) and contributor(s) and not of MDPI and/or the editor(s). MDPI and/or the editor(s) disclaim responsibility for any injury to people or property resulting from any ideas, methods, instructions or products referred to in the content.